Current Optics and Photonics
Vol. 1, No. 6, December 2017, pp. 598-603

ISSN: 2508-7266(Print) / ISSN: 2508-7274(Online)
DOI: https://doi.org/10.3807/COPP.2017.1.6.598

A Novel 3-D Imaging Configuration Exploiting Synthetic Aperture Ladar

Liang Guo[1]*, Yinli Huang[1], Xiaozhen Li[2], Xiaodong Zeng[1], Yu Tang[3], and Mengdao Xing[3]

[1]*School of Physics and Optoelectronic Engineering, Xidian University, Xi'an 710071, China*
[2]*Kunming University, Kunming 650214, China*
[3]*National Lab. of Radar Signal Processing, Xidian University, Xi'an, 710071, China*

(Received September 10, 2017 : revised October 30, 2017 : accepted November 14, 2017)

Traditional three-dimensional (3-D) laser imaging systems are based on real aperture imaging technology, whose resolution decreases as the range increases. In this paper, we develop a novel 3-D imaging technique based on the synthetic aperture technology in which the imaging resolution is significantly improved and does not degrade with the increase of the range. We consider an imaging laser radar (ladar) system using the floodlight transmitting mode and multi-beam receiving mode. High 3-D imaging resolutions are achieved by matched filtering the linear frequency modulated (LFM) signals respectively in range, synthetic aperture along-track, and the real aperture across-track. In this paper, a novel 3-D imaging signal model is given first. Because of the motion during the transmission of a sweep, the Doppler shift induced by the continuous motion is taken into account. And then, a proper algorithm for the 3-D imaging geometry is given. Finally, simulation results validate the effectiveness of the proposed technique.

Keywords : Ladar, Synthetic aperture, 3-D imaging
OCIS codes : (110.6880) Three-dimensional image acquisition; (280.3640) Lidar

I. INTRODUCTION

Imaging laser radar (ladar) is an active remote sensing system that is widely used in various military and civilian applications, such as forest resource estimation [1, 2], digital city [3], hazard assessment [4], flood defence [5], and pipeline mapping [6]. Imaging ladar has attracted increasing attention because of its high resolution and high positioning accuracy. So far, a number of mature three-dimensional (3-D) imaging ladar systems have been developed, such as SHOALS, MAPLA, ALTM, TOPSYS, Nakanihon, ASLRIS, and the 863 push broom system [7].

Imaging ladars have two main working modes: scanning [8] and push broom. The scanning mode regularly controls the laser beam scanning over ground and detects the laser echo by a plane rotating mirror, a plane mirror, or multiple mirrors. This mode requires the system to have a higher pulse repetition frequency (PRF). A push broom laser 3-D imaging system adopts array transceiver mode in across-track and scanning the along-track provided by the platform itself in order to realize 3-D target imaging so as to reduce the required PRF. However, both scanning and push broom imaging ladar systems use the real apertures offered by the ladar. As such, their resolution decreases as the range increases.

By analysing the Doppler characteristics of the echo signal, the synthetic aperture technique forms a long synthetic aperture, so that the along-track resolution is significantly enhanced and is independent of the range [9]. While synthetic aperture technology is mature in microwave radar [9, 10], synthetic aperture ladar (SAL) is relatively new and is a subject of hot research activities. So far, several indoor and airborne SAL systems have been successfully developed [11-17], and it is expected that the synthetic aperture technology will be more popularly applied in laser 3-D imaging systems.

In this paper, we propose a novel 3-D imaging ladar system exploiting the synthetic aperture technology, and signal model is analyzed to propose an appropriate data processing algorithm. Inspired by the broom imaging ladar

*Corresponding author: lguo@mail.xidian.edu.cn, ORCID 0000-0001-6296-6028
Color versions of one or more of the figures in this paper are available online.

system, we adopt the floodlight illumination [18] mode in the transmitter and a linear array in the receiver. Frequency Modulated Continuous Wave (FMCW) signals are used as the transmitting signal and matched filtering is applied to achieve a high resolution of the height. Synthetic technology is used along-track to analyse the Doppler characteristics of the echoes in order to increase the along-track resolution, whereas a real aperture imaging method is used across-track.

This paper is organized as follows: The downward-looking 3-D imaging model of the synthetic aperture ladar is described in Section 2. The proposed signal processing method is presented in Section 3. In Section 4 simulation experiments are provided to verify the effectiveness of the proposed algorithm. Finally, the summary of this paper is given in Section 5.

II. DOWNWARD-LOOKING 3-D IMAGING MODEL

In a push broom 3-D imaging configuration, the downward-looking 3-D imaging model of SAL is showed in Fig. 1. The platform flies at a constant speed v along the Y-axis in a straight line and its height is h. The ladar adopts the laser floodlight transmitting mode and the multi-beam receiving mode. The across-track and along-track align with the X-axis and the Y-axis, respectively, whereas the Z-axis defines the height direction.

The ladar uses a frequency modulated continuous wave (FMCW) signal as the transmitting signal and its signal form is expressed as:

$$s\left(\hat{t},t_m\right)=\mathrm{rect}\left(\frac{\hat{t}}{T_p}\right)\exp\left(j2\pi f_c t+j\pi\gamma\hat{t}^2\right) \tag{1}$$

where f_c is the carrier frequency, T_p is the pulse repetition interval (PRI), γ is the frequency modulation rate, $\hat{t}$ is the fast time in range, and $t_m=mT_p$ $(m=1,2,3,...)$ is the slow time in azimuth, which is the starting time of each signal, and $t=t_m+\hat{t}$ is the full time.

The echo from a target $P\left(x_0,y_0,z_0\right)$ located in the imaging scene can be expressed as:

$$s\left(\hat{t},t_m\right)=\mathrm{rect}\left(\frac{\hat{t}-R\left(\hat{t},t_m\right)/c}{T_p}\right)\exp\left(j2\pi f_c\left(t-\frac{R\left(\hat{t},t_m\right)}{c}\right)+j\pi\gamma\left(\hat{t}-\frac{R\left(\hat{t},t_m\right)}{c}\right)^2\right) \tag{2}$$

where c is the propagation velocity of light, and $R\left(\hat{t},t_m\right)$ is the round-trip slant range between the point target and the transmit-receive lens. $R\left(\hat{t},t_m\right)$ can be expressed as $R\left(\hat{t},t_m\right)=R_T\left(\hat{t},t_m\right)+R_R\left(\hat{t},t_m\right)$, in which

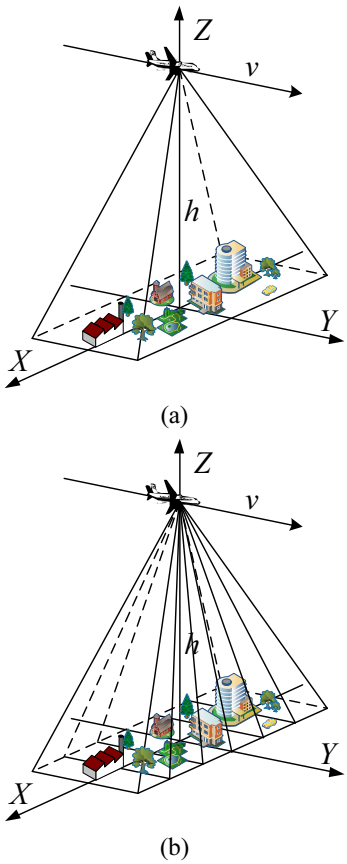

FIG. 1. Transmitting and receiving modes of downward-looking 3-D imaging: (a) floodlight illumination mode; (b) multi-beam receiving mode.

$$\begin{cases}R_T\left(\hat{t},t_m\right)=\sqrt{x_0^2+\left(vt_m+v\hat{t}-y_0\right)^2+\left(h-z_0\right)^2}\\ R_R\left(\hat{t},t_m\right)=\sqrt{\left(x_R-x_0\right)^2+\left(vt_m+v\hat{t}-y_0\right)^2+\left(h-z_0\right)^2}\end{cases} \tag{3}$$

and x_R is the position of the receiving lens in the X axis. Considering the continuous motion of the platform in the process of transmitting and receiving signals, the slant range of Eq. (3) is related to the fast time $\hat{t}$.

In order to remove the double square root form in the instantaneous slant range, the equivalent phase center principle is used. That is, when compared to the work range, the length of the baseline between the two bistatic lenses is very short so that the work mode can be treated as a single-lens mode in the middle of the two lenses, which can be considered as a transmit-receive lens, but a constant phase [19] should be compensated. The range between the equivalent phase center and scene center point P can be expressed as

$$R'\left(\hat{t},t_m\right)=\sqrt{\left(x_R/2-x_0\right)^2+\left(vt_m+v\hat{t}-y_0\right)^2+\left(h-z_0\right)^2} \quad (4)$$

We perform coherent signal reception in the time domain using the following dechirping function to reduce the data size:

$$H_{dechirp}\left(\hat{t},t_m\right)=\mathrm{rect}\left(\frac{\hat{t}-2R_{ref}/c}{T_p}\right)\exp\left(-j2\pi f_c\left(t-\frac{2R_{ref}}{c}\right)-j\pi\gamma\left(\hat{t}-\frac{2R_{ref}}{c}\right)^2\right) \quad (5)$$

where R_{ref} is the reference slant range. After the dechirping process, the differential signal becomes

$$s\left(\hat{t},t_m\right)=\exp\left(-j\frac{4\pi}{c}f_cR_\Delta\right)\exp\left(-j\frac{4\pi}{c}\gamma\left(\hat{t}-\frac{2R_{ref}}{c}\right)R_\Delta\right)\exp\left(j\frac{4\pi}{c^2}\gamma R_\Delta{}^2\right) \quad (6)$$

where $R_\Delta=R'\left(\hat{t},t_m\right)-R_{ref}$.

In Eq. (5), the magnitude is ignored because it does not affect the imaging. The first exponential term is the phase history in azimuth, the second one is single-frequency signal related to the position in range, and the third one is the residual video phase (RVP). The RVP will affect the Doppler phase so it must be compensated [20]. In the subsequent derivation, we assume that the RVP term is properly compensated.

III. PROPOSED IMAGING ALGORITHM

In this paper, the imaging model uses a pulse compression technique to achieve a high resolution in height, adopts a synthetic aperture technique to improve the resolution along-track, and uses a linear array detector to achieve a high across-track resolution. Therefore, the signal processing in the height and along-track directions should be analyzed in detail.

3.1. Doppler Frequency Shift Analysis and Correction

Because of a long sweep period, the motion of the platform in a transmission sweep period must be taken into account, so the slant range in Eq. (4) is related to the fast time. The slant range can be expressed by applying Taylor series expansion for Eq. (4), expressed as

$$R'\left(\hat{t},t_m\right)\approx R'\left(t_m\right)+\frac{v\left(vt_m-y_0\right)}{R'\left(t_m\right)}\hat{t} \quad (7)$$

where $R'\left(t_m\right)=\sqrt{\left(x_R/2-x_0\right)^2+\left(vt_m-y_0\right)^2+\left(h-z_0\right)^2}$.

According to Eq. (7), the Doppler frequency shift introduced by the platform continuous motion is

$$f_d=-\frac{2}{\lambda}\frac{dR'\left(\hat{t},t_m\right)}{d\hat{t}}=-\frac{2}{\lambda}\frac{v\left(vt_m-y_0\right)}{R'\left(t_m\right)} \quad (8)$$

where λ is the wavelength corresponding to the center frequency.

Considering the working geometry, $\frac{vt_m-y_0}{R'\left(t_m\right)}=-\sin\theta$, where θ is the instantaneous observation angle of the point target, the frequency shift can be expressed as

$$f_d=-\frac{2}{\lambda}\frac{v\left(vt_m-y_0\right)}{R'\left(t_m\right)}=-\frac{2v}{\lambda}\left(-\sin\theta\right)=f_a \quad (9)$$

where f_a is the Doppler frequency.

With Eq. (7), Eq. (6) can be represented as

$$s(\hat{t},t_m)=\exp\left(-j\frac{4\pi}{\lambda}\left(R'(t_m)-R_{ref}\right)\right)\exp\left(-j\frac{4\pi}{c}\gamma\left(\hat{t}-\frac{2R_{ref}}{c}\right)\left(R'\left(t_m\right)-R_{ref}\right)\right)\exp\left(j2\pi f_a\hat{t}\right) \quad (10)$$

where the third exponential term is the Doppler frequency shift in range introduced by the continuous motion of the platform. The Doppler frequency shift will change the focused position of the target in range. Because it is related to the azimuth frequency, the Doppler frequency shift will be considered as a residue of the range cell migration after range pulse compression. Meanwhile, the change in the target focused position will lead to mismatching in the process of azimuth compression. Therefore, the frequency shift must be compensated, which can be done in the azimuth Doppler domain.

The signal can be transformed into the azimuth frequency domain based on the principle of stationary phase [9], expressed as

$$S\left(\hat{t},f_a\right)=\exp\left(-j4\pi R_{Bi}\sqrt{\left(\frac{1}{\lambda}+\frac{\gamma}{c}\left(\hat{t}-\frac{2R_{ref}}{c}\right)\right)^2-\left(\frac{f_a}{2v}\right)^2}\right)\exp\left(-j2\pi\frac{y_0}{v}f_a\right)\exp\left(j4\pi\left(\frac{1}{\lambda}+\frac{\gamma}{c}\left(\hat{t}-\frac{2R_{ref}}{c}\right)\right)R_{ref}\right)\exp\left(j2\pi f_a\hat{t}\right) \quad (11)$$

where $R_{Bi}=\sqrt{\left(x_R/2-x_0\right)^2+\left(h-z_0\right)^2}$ is the nearest range between the i th path and the point target.

From Eq. (11), the correction function of the Doppler frequency shift can be expressed as

$$H_{DFS}\left(\hat{t},f_a\right)=\exp\left(-j2\pi f_a\hat{t}\right) \tag{12}$$

By multiplying Eq. (11) by Eq. (12), the output can be expressed as

$$\begin{aligned}S'\left(\hat{t},f_a\right)=&\exp\left(-j4\pi R_{Bi}\sqrt{\left(\frac{1}{\lambda}+\frac{\gamma}{c}\left(\hat{t}-\frac{2R_{ref}}{c}\right)\right)^2-\left(\frac{f_a}{2v}\right)^2}\right)\\&\exp\left(j4\pi\left(\frac{1}{\lambda}+\frac{\gamma}{c}\left(\hat{t}-\frac{2R_{ref}}{c}\right)\right)R_{ref}\right)\\&\exp\left(-j2\pi\frac{y_0}{v}f_a\right)\end{aligned} \tag{13}$$

3.2. Processing in Height Direction

In order to complete Range Cell Migration (RCM) correction and compression in the height direction, the first exponential term in Eq. (13) is expanded on $\left(\hat{t}-\frac{2R_{ref}}{c}\right)$ by Taylor series expansion as

$$\begin{aligned}&\sqrt{\left(\frac{1}{\lambda}+\frac{\gamma}{c}\left(\hat{t}-\frac{2R_{ref}}{c}\right)\right)^2-\left(\frac{f_a}{2v}\right)^2}\approx\phi_0\left(f_a\right)\\&+\phi_1\left(f_a\right)\left(\hat{t}-\frac{2R_{ref}}{c}\right)+\phi_2\left(f_a\right)\left(\hat{t}-\frac{2R_{ref}}{c}\right)^2\end{aligned} \tag{14}$$

where

$$\phi_0\left(f_a\right)=\sqrt{\left(\frac{1}{\lambda}\right)^2-\left(\frac{f_a}{2v}\right)^2} \tag{14a}$$

$$\phi_1\left(f_a\right)=\frac{\gamma}{c\lambda\sqrt{\left(\frac{1}{\lambda}\right)^2-\left(\frac{f_a}{2v}\right)^2}} \tag{14b}$$

$$\phi_2\left(f_a\right)=-\frac{\left(\frac{\gamma}{c}\right)^2\left(\frac{f_a}{2v}\right)^2}{2\left(\sqrt{\left(\frac{1}{\lambda}\right)^2-\left(\frac{f_a}{2v}\right)^2}\right)^3} \tag{14c}$$

Here, the third and higher-order terms are ignored. In this expression, $\phi_0\left(f_a\right)$ is the phase term along-track, and $\phi_1\left(f_a\right)$ is the coupling phase in the height direction and along-track, and $\phi_2\left(f_a\right)$ is a secondary pulse compression term. According to Eq. (14), the migration correction and the secondary pulse compression function can be expressed as

$$\begin{aligned}H_{RCMC,SC}=&\exp\left(j4\pi R_{B0}\left(\phi_1\left(f_a\right)\left(\hat{t}-\frac{2R_{ref}}{c}\right)+\phi_2\left(f_a\right)\left(\hat{t}-\frac{2R_{ref}}{c}\right)^2\right)\right)\\&\exp\left(-j\frac{4\pi\gamma}{c}R_{B0}\left(\hat{t}-\frac{2R_{ref}}{c}\right)\right)\end{aligned} \tag{15}$$

The effect of the third exponential term in Eq. (15) is to ensure that the target position does not change after focusing in the height direction. In addition, R_{Bi} in the range migration correction and the secondary pulse compression reference function are all approximated by the nearest range R_{B0} corresponding to the target on the ground plane underneath the platform. After the range migration correction and the secondary pulse compression, the signal is dechirpped and converted into the range frequency domain. In other words, this step is equivalent to achieving the pulse compression in the height direction.

After the pulse compression in the height direction, the signal becomes

$$\begin{aligned}S\left(f_r,f_a\right)=&\exp\left(-j4\pi R_{Bi}\sqrt{\left(\frac{1}{\lambda}\right)^2-\left(\frac{f_a}{2v}\right)^2}\right)\\&\exp\left(-j2\pi\frac{y_0}{v}f_a\right)\\&\operatorname{sinc}\left(\pi T_p\left(f_r+\frac{2\gamma}{c}\left(R_{Bi}-R_{ref}\right)\right)\right)\\&\exp\left(-j\frac{4\pi R_{ref}}{c}f_r\right)\end{aligned} \tag{16}$$

In order to preserve the phase while processing in the height direction, we need to compensate the final exponential term in Eq. (16) using the following compensation function:

$$H_{PMF}\left(f_r\right)=\exp\left(j\frac{4\pi R_{ref}}{c}f_r\right) \tag{17}$$

3.3. Along-track Compression

After the completion of the phase compensation in range, the pulse compression in azimuth can be performed with the following reference function in azimuth:

$$H_{az}\left(f_a\right)=\exp\left(j4\pi R_{Bi}\sqrt{\left(\frac{1}{\lambda}\right)^2-\left(\frac{f_a}{2v}\right)^2}\right). \tag{18}$$

According to Eq. (16), the point target in the height direction is focused at the nearest range instead of the actual target height. Therefore, we need to perform the corresponding projection transformation according to the geometric relations of each detector and to project the focused point target to their real positions.

IV. SIMULATION RESULTS

In this section, we present simulation results to validate the downward-looking 3-D imaging configuration and the imaging algorithm of synthetic aperture ladar proposed in this paper. The simulation parameters are given in Table 1.

TABLE 1. Simulation parameters

Parameter	Value
Carrier wavelength/μm	1.5
Signal bandwidth/GHz	6
Aperture of the transmitter/cm	0.8 × 0.2 (C × A)
Number of the receiving elements	65
Pulse repetition interval/μs	50
Sampling frequency/MHz	20
Flight altitude/km	2
Velocity/(m/s)	60

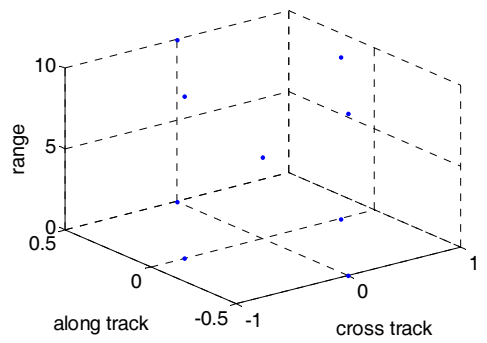

FIG. 2. Display of the points.

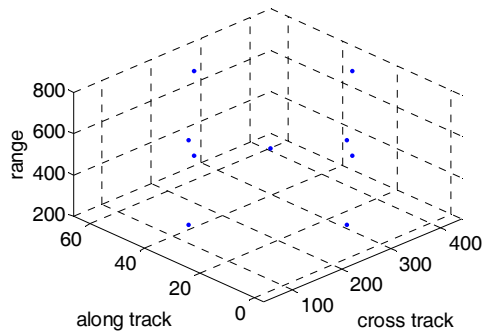

FIG. 3. Imaging results of the points.

The simulation scene setting is shown in Fig. 2, where nine point targets are distributed in three levels, i.e., four points in the plane ground, one point in the height of 5 m and four points in the height of 10 m.

The imaging results are shown in Fig. 3. The positions of the point targets after imaging are basically the same as those in the original scene, thus verifying the effectiveness of the proposed algorithm.

In order to further verify the proposed algorithm, the imaging result of the point targets in position zero across-track is analyzed and shown in Fig. 4. Figure 4(a) shows the imaging result of the slice position, whereas Figs. 4(b) and 4(c) depict the contour map of points A and B depicted in Fig. 4(a). It is observed that the main lobe and the side lobes are clearly separated, thus validating this algorithm.

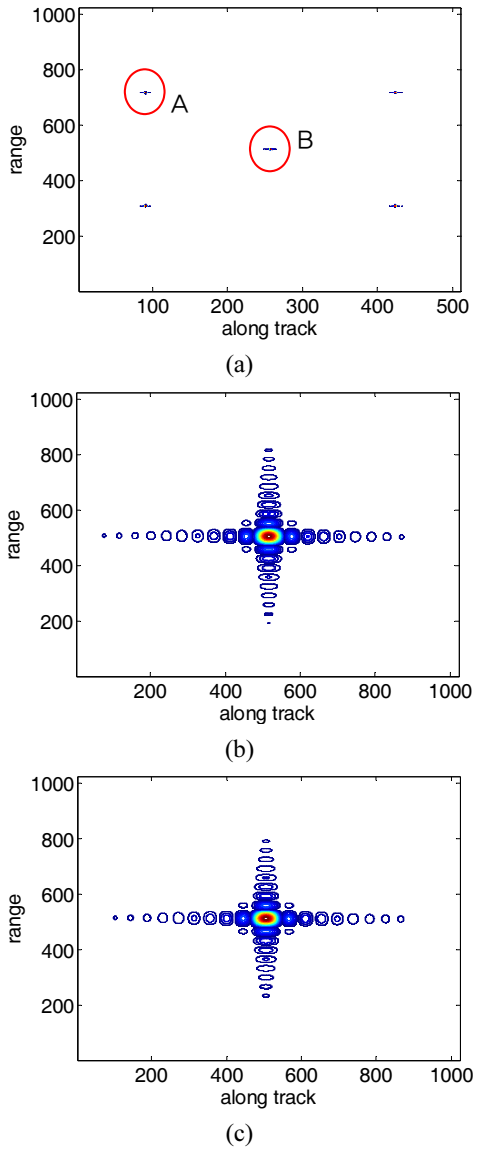

FIG. 4. Imaging results of the given algorithm: (a) Image result; (b) point A; (c) point B.

V. CONCLUSION

Synthetic aperture ladar is an effective means for long-distance active imaging in remote sensing. In this paper, we have developed a laser 3-D imaging system based on synthetic aperture technology, and its effectiveness was verified by simulation results.

ACKNOWLEDGMENT

National Natural Science Foundation of China (NSFC) (61001211, 61303035, 61471283, 61475122, 61772397); the Fundamental Research Funds for the Central Universities (NSIY171412); National Key Scientific Instrument and Equipment Development Project (2013YQ310633); Natural Science Fundamental of Shaanxi Province (2017JQ6021).

REFERENCES

1. M. Nilsson, "Estimation of tree height and stand volume using an airborne LiDAR system," Remote Sens. Environ. **56**(1), 1-7 (1996).
2. G. Sun and K. J. Ranson, "Modeling lidar returns from forest canopies," IEEE Trans. Geosci. Remote Sens. **38**(6), 2617-2626 (2000).
3. S. Filin, "Surface classification from airborne laser scanning data," Comput. Geosci. **30**, 1033-1041 (2004).
4. M. Janeras, M. Navarro, G. Arnó, A. Ruiz, W. Kornus, J. Talaya, M. Barberà, and F. López, "Lidar applications to rock fall hazard assesment in vall de núria," *4th ICA Mountain Cartography Workshop Vall de Núria*, 1-14 (2004).
5. T. Burton and D. Scott, *LIDAR for flood defence*, http://www.bks.co.uk/en/press_archive.html.
6. C. V. Tao and Y. Hu, "Assessment of airborne lidar imaging technology for pipeline mapping and safety applications," *Pecora 15/Land Satellite Information IV/ISPRS Commission I/FIEOS 2002 Conference Proceedings*.
7. H. Min, H. Yihua, Z. Nanxiang, and L. Wei, "Application of airborne three-dimensional laser imaging." Laser Optoelectron. Prog. **3**, 43-49 (2008).
8. M. Yao, "Study on laser scanning imaging system," Changchun: Changchun University of Science and Technology (2012).
9. I. G. Cumming and F. H. Wong, "Digital processing of synthetic aperture radar data: algorithms and implementation," Norwood, MA: Artech House (2005).
10. Z. Bao, M.-D. Xing, and T. Wang, "Radar imaging techniques," Beijing: Publishing House of Electronics Industry (2005).
11. M. Bashkansky, R. L. Lucke, E. Funk, L. J. Rickard, and J. Reintjes, "Two-dimensional synthetic aperture imaging in the optical domain," Opt. Lett. **27**, 1983-1985 (2002).
12. S. M. Beck, J. R. Buck, W. F. Buell, R. P. Dickinson, D. A. Kozlowski, N. J. Marechal, and T. J. Wright, "Synthetic aperture imaging ladar: laboratory demonstration and signal processing," Appl. Opt. **44**, 7621-7629 (2005).
13. L. Guo, M. Xing, L. Zhang, Y. Tang, and Z. Bao, "Research on indoor experimentation of range SAL imaging system," Sci. China, Ser. E: Technol. Sci. **10**, 3098-3104 (2009).
14. Y. Zhou, N. Xu, Z. Luan, A. Yan, L. Wang, J. Sun, and L. Liu, "2D imaging experiment of a 2D target in a laboratory-scale synthetic aperture imaging ladar," Acta Opt. Sin. **29**, 2030-2032 (2009).
15. L. Liu, Y. Zhou, Y. Zhi, J. Sun, Y. Wu, Z. Luan, A. Yan, L.Wang, E. Dai, and W. Lu, "A large-aperture synthetic aperture imaging ladar demonstrator and its verification in laboratory space," Acta Opt. Sin. **31**, 0900112 (2011).
16. J. Ricklin, M. Dierking, S. Fuhrer, B. Schumm, and D. Tomlison, "Synthetic aperture ladar for tactical imaging (SALTI) flight test results and path forward," Presented at the Coherent Laser Radar Conferences, Snowmass, Colorado, USA, 9-13 July 2007.
17. B. Krause, J. Buck, C. Ryan, D. Hwang, P. Kondratko, A. Malm, A. Gleason, and S. Ashby, "Synthetic aperture ladar flight demonstration," in *CLEO: 2011- Laser Applications to Photonic Applications, Technical Digest* (CD) (Optical Society of America, 2011), paper PDPB7.
18. N. D. Hardy and J. H. Shapiro, "Computational ghost imaging versus imaging laser radar for three-dimensional imaging," Phys. Rev. A **87**, 023820-1-11 (2013).
19. W. Jing, M. Xing, C.-W. Qiu, Z. Bao, and T.-S. Yeo, "Unambiguous reconstruction and high-resolution imaging for multiple-channel SAR and airborne experiment results," IEEE Geosci. Remote Sens. Lett. **6**, 102-106 (2009).
20. A. Meta, P. Hoogeboom, and L. P. Ligthart, "Signal processing for FMCW SAR," IEEE Trans. Geosci. Remote Sens. **45**, 3519-3532 (2007).